

3D microstructure evolution in Na_xFePO_4 storage particles for sodium-ion batteries

Tao Zhang^{a,*}, Mohsen Sotoudeh^b, Axel Groß^{b,c}, Robert M. McMeeking^{d,e,f}, Marc Kamlah^a

^a Institute for Applied Materials, Karlsruhe Institute of Technology, 76344 Eggenstein-Leopoldshafen, Germany

^b Institute of Theoretical Chemistry, Ulm University, 89069 Ulm, Germany

^c Helmholtz Institute Ulm (HIU), Electrochemical Energy Storage, 89069 Ulm, Germany

^d Materials Department and Department of Mechanical Engineering, University of California, Santa Barbara, CA 93106, USA

^e School of Engineering, University of Aberdeen, King's College, Aberdeen AB24 3UE, Scotland, UK

^f INM-Leibniz Institute for New Materials, 66123 Saarbrücken, Germany

HIGHLIGHTS

- A 3D electro-chemo-mechanical phase-field model based on first-principles.
- Elastic anisotropy of Na_xFePO_4 is determined for the first time.
- 1D Na diffusion channels lead to a kinetically arrested state.
- Defect-actuated in-plane diffusion induces low-energy [100] intercalation-wave.
- The double wave propagation along [010] is more prone to particle cracking.

ARTICLE INFO

Keywords:

Sodium-ion batteries
Microstructure evolution
Anisotropic elasticity
Phase-field approach
First-principles

ABSTRACT

The cathode material Na_xFePO_4 of sodium-ion batteries exhibits complex phase segregation thermodynamics with the existence of an intermediate phase, and large volume change during (dis)charging. A virtual multiscale modeling chain is established to construct a 3D anisotropic electro-chemo-mechanical phase-field model based on first-principles calculations for Na_xFePO_4 , which considers phase changes, electrochemical reactions, anisotropic diffusion, anisotropic misfit strain, and anisotropic elasticity, as well as the concentration-dependence of the elasticity tensor. The elastic properties of Na_xFePO_4 are determined by first-principles for the first time. We investigate how surface reaction kinetics and crystal anisotropy influence the full 3D microstructure evolution, with results that include phase evolution, interface morphology, and stress evolution in Na_xFePO_4 particles. We find that the existence of 1D Na diffusion channels leads to a kinetically arrested state of single wave propagation along [010]. Furthermore, defect-actuated in-plane diffusion induces low-energy single wave propagation along [100] controlled by the concentration dependent anisotropic elasticity tensor. In addition, the morphology of the double wave propagation along [010] is more prone to particle cracking and mechanical degradation. Beyond Na_xFePO_4 , the findings of this work point towards opportunities to engineer desired phase behavior with better mechanical stability by defect-actuated out-of-1D diffusion of an intercalation electrode material.

1. Introduction

Intercalation electrode materials commonly exhibit phase changes during regular operation. One aspect that has attracted attention is how to model the complex thermodynamics of phase segregation of electrode materials and to elucidate the interaction between microstructure evolution and mechanics. On the one hand, the mechanics plays a nontrivial role in phase evolution, leading to a variety of phase morphologies, e.g., as observed in olivine LiFePO_4 [1–3], a widely

used cathode material for lithium ion batteries (LIBs). LiFePO_4 possesses strong anisotropies of diffusion [4] and elasticity [5]. On the other hand, interphase morphology within single particles is directly related to possible degradation mechanisms of the battery. The respective phases of such an electrode material have different lattice constants which, in turn, induces large concentration gradients at a mesoscopic scale and also large stress magnitudes. These phenomena lead to particle cracking and capacity loss [6–15].

* Corresponding author.

E-mail address: tao.zhang@kit.edu (T. Zhang).

Over the past decades LIBs have attracted intensive attention for electrochemical energy storage. The current enormous utilization of LIBs combined with the limited availability of lithium and its uneven international distribution is subject of serious concern. In contrast to lithium, sodium is widely available throughout the world, is abundant, is low cost. Thus, sodium ion batteries (NIBs), having comparable energy density [16–18], become a potential promising alternative to LIBs. Olivine NaFePO_4 becomes one of the best candidates for the cathode materials of NIBs due to its higher voltage, higher theoretical specific capacity, and thermal stability [19]. Although olivine NaFePO_4 exhibits the same crystal structure as olivine LiFePO_4 [20,21], its phase segregation thermodynamics is quite different. In contrast to Li_xFePO_4 (LiFPO), where transformation from a low concentration phase, FePO_4 , into a high concentration phase, LiFePO_4 , and vice versa occurs directly [22], Na_xFePO_4 (NaFPO) goes through an intermediate state, $\text{Na}_{2/3}\text{FePO}_4$ [23] upon transforming from the sodium poor to the sodium rich phase and vice versa. At room temperature, for $0 < x < 2/3$, phase segregation of NaFPO into a low concentration phase FePO_4 and a high concentration phase $\text{Na}_{2/3}\text{FePO}_4$ is suitable. A single phase region is favorable for $2/3 < x < 1$. In addition, the volume change between FePO_4 and NaFePO_4 is about 17%, and even the volume extension from the sodium poor phase to the intermediate state is nearly 2 times that for LiFPO upon full lithiation [23]. Amorphization and slower Na^+ diffusion in the cathode of NaFPO could lead to additional strain development compared to its lithium counterpart [24]. Based on the combination of in situ strain measurements with the theoretical model, Özdogru et al. [25] recently studied the rate dependent mechanical response of NaFPO cathodes. It is found that NaFPO exhibits asymmetrical strains between insertion and extraction, as well as smaller strain at lower charging rates.

Phase separation causes spatial heterogeneity, which entangles the interpretation of experimental observations and usually obviates the classical assumption of a core shell structure, e.g., for LiFPO [26–29]. Thermodynamic phase field modeling can be a consistent and accurate option to describe phase changes accompanied by diffusion. A Cahn Hilliard phase field model, which is weakly nonlocal [30], depends on a continuous order parameter, leading to diffuse interfaces between phases without the troublesome tracking of the sharp interface position [31]. Although many intercalation electrode materials exhibit phase separation, phase field models have been nearly merely focused on LiFPO [1, 3,32–37]. Until now, all phase field simulations of NaFPO have been limited to isotropic simplifications for diffusion and mechanics, and also limited to 1D or 2D for a quasistatic insertion process [38–41]. A phase field model for NaFPO was investigated for the first time for a spherically symmetric boundary value problem [38]. However, the phase field model [38] is based on the standard regular solution function [42,43]. Recently, a multiwell potential for NaFPO for the full range of sodium concentration has been constructed by fitting to an experimental open circuit voltage, and then used to investigate 2D phase evolution during the whole process of sodiation [41]. It was found that the appearance of an intermediate phase not only explains the phenomenon of varying solubility limits but also causes a decrease in sodiation stress magnitudes. To our knowledge, neither experimental reports nor theoretical works have revealed the full 3D microstructure evolution for NaFPO, and thus have not addressed 3D phase evolution, anisotropic phase boundary morphologies, and stress generation in 3D.

The evolution of phase segregation and the underlying mechanisms in intercalation materials are difficult to ascertain due to the intricate phase morphologies observed. Once the nucleation energy barrier is overcome, phase nucleation is spontaneous, but it is difficult to observe phase nucleation experimentally [33]. Also, it is a computational challenge to resolve the complex moving interface morphologies during phase change in intercalation materials in a satisfactorily accurate way due to the fact that the initiation and subsequent development of phase nucleation may happen in a relatively rapid manner compared to the diffusion process. What is more, in order to accurately describe the

non equilibrium behavior in terms of anisotropic phase boundary morphologies and stresses, crystal anisotropy has to be taken into account for intercalation electrode materials, including anisotropic diffusion, anisotropic misfit strain, as well as anisotropic elasticity.

Anisotropic phase field models have been almost entirely focused on LiFPO. Singh et al. [32] developed a 2D depth averaged model without mechanics, and predicted the $\text{LiFePO}_4/\text{FePO}_4$ phase boundary to propagate along [100] like a “travelling wave”. This depth averaged approximation applies to thin plate like particles where diffusion in channels along [101] is much quicker than surface reactions, leading to a quasi equilibrium lithium composition distribution along [010]. Cogswell and Bazant [1] subsequently incorporated elastic strain energy into the 2D depth averaged model using elastic constants independent of both the lithium concentration and the material phase, to study the influence of stresses on the phase morphology in square LiFPO particles. Their anisotropic elasticity tensor and misfit strain analysis predicted that [101] phase boundary is energetically favorable, and they attributed experimental observation of [100] phase boundary [26,28] to a fractional loss of misfit strain in [001], resulting from dislocations or cracks. However, they performed their phase field simulations by considering just relaxation at constant average lithium concentration, rather than phase evolution during a time dependent insertion process.

A close inspection of the complicated phase morphologies from experiments shows that it is necessary to carry out full 3D simulations with the appropriate anisotropies accounted for. To the best of our knowledge, no works have studied full 3D anisotropic phase field simulations of NaFPO, and even for LiFPO there are only a few corresponding studies. Welland et al. [35] developed a 3D chemo mechanical phase field model and investigated the steady states of spherical LiFPO crystals. However, the electrochemical reaction often described by the Butler Volmer equation is not taken into account in their model. For these 3D phase field models for LiFPO [2,3], the elasticity tensor is assumed to be independent of composition, taken to be the average values of the elasticity tensors of LiFePO_4 and FePO_4 . Moreover, the generation of stresses in 3D has not yet been investigated during insertion/extraction in the 3D phase field models described above [2,3,35].

In this work, a 3D anisotropic electro chemo mechanical phase field model is developed, accounting for phase changes including nucleation and spinodal decomposition, electrochemical reactions, anisotropic diffusion, anisotropic misfit strain, and anisotropic elasticity, as well as the concentration dependence of the elasticity tensor. At present, there are no available experimental data on the elastic properties of NaFPO. Here, a virtual multiscale modeling chain is established to construct an anisotropic electro chemo mechanical model based on first principles calculations for NaFPO. For this purpose, the elastic properties of NaFPO are calculated from first principles for the first time. In addition, based on an open circuit voltage calculated by first principles, as well, a multiwell potential is determined for Na_xFePO_4 , accounting for both two phase segregation between FePO_4 and $\text{Na}_{2/3}\text{FePO}_4$ and the single phase region. We investigate how kinetic competition between surface reactions and diffusion, as well as crystal anisotropy influence the full 3D microstructure evolution of NaFPO, and capture the dynamics for four different phase separating processes. We envision that a desired phase behavior with better mechanical stability, and thus better battery performance, may be achieved by defect actuated out of 1D diffusion for an intercalation electrode material.

2. Methods

2.1. A virtual multiscale modeling chain

2.1.1. First principles calculations

All first principles calculations were performed in the framework of density functional theory (DFT) [44,45] employing the Projector

Augmented Wave (PAW) [46] method as implemented in the Vienna *Ab initio* Simulation Package (VASP) [47–49]. The exchange correlation effects were described by the generalized gradient approximation (GGA) using the Perdew Burke Ernzerhof (PBE) functional [50]. In the calculations, to properly describe the localized (strongly correlated) d electrons, the U parameters [51] in the d orbitals are set to $U_{\text{FePO}_4} = 5.90$ eV and $U_{\text{NaFePO}_4} = 4.70$ eV. The exchange constant $J = 1$ eV is used for both compounds. The calculations were optimized using $4 \times 6 \times 6$ k point mesh, with a plane wave cutoff of 600 eV, and a convergence within 1×10^{-5} eV per supercell. The atomic positions and volume are relaxed without any restriction.

Na_xFePO_4 compounds are simulated in orthorhombic olivine structures, having $Pnma$ space group, consisting of sixfold coordinated Fe ions surrounded by oxygen atoms forming layers of edge sharing octahedra and four fold coordinated P ions as an interlayer. The experimental lattice parameters of FePO_4 are taken from [52] ($a = 9.7599$ Å, $b = 5.7519$ Å, and $c = 4.7560$ Å).

For all calculations, a C type antiferromagnetic configuration is chosen for the magnetic ground state structure. We have applied symmetric distortion matrices to the equilibrium unit cell of NaFePO_4 and FePO_4 containing four formula units for elastic constants. The time step for ionic motion has been set to 0.015 to minimize the influence of higher order terms on the elastic constants.

The bulk modulus K , shear modulus G , and Young's modulus E are estimated from the calculated elastic constants c_{ij} ($i, j = 1, \dots, 6$), according to the Voigt, Reuss, and Hill approximations. Based on the Voigt approximation, the bulk modulus and shear modulus are given by

$$K_V = \frac{1}{9}(c_{11} + c_{22} + c_{33}) + \frac{2}{9}(c_{12} + c_{13} + c_{23}), \quad (1)$$

$$G_V = \frac{1}{15}(c_{11} + c_{22} + c_{33} - c_{12} - c_{13} - c_{23}) + \frac{1}{5}(c_{44} + c_{55} + c_{66}). \quad (2)$$

According to the Reuss approximation, the bulk and shear moduli are expressed by

$$K_R = \frac{1}{(s_{11} + s_{22} + s_{33}) + 2(s_{12} + s_{13} + s_{23})}, \quad (3)$$

$$G_R = \frac{1}{4(s_{11} + s_{22} + s_{33}) - 4(s_{12} + s_{13} + s_{23}) + 3(s_{44} + s_{55} + s_{66})}, \quad (4)$$

using the compliance tensor \mathbf{S} which is calculated as the inverse of the elasticity tensor, $\mathbf{S} = \mathbf{C}^{-1}$.

The upper and lower limits of the true polycrystalline modulus are represented by the Voigt and Reuss approximations. The arithmetic mean values of Voigt's and Reuss's moduli is raised by Hill

$$K_H = \frac{1}{2}(K_R + K_V), \quad (5)$$

$$G_H = \frac{1}{2}(G_R + G_V). \quad (6)$$

The Young's modulus E and Poisson's ratio ν are given by

$$E = \frac{9KG}{3K + G}, \quad (7)$$

$$\nu = \frac{3K - 2G}{2(3K + G)}. \quad (8)$$

2.1.2. Anisotropic electro chemo mechanical phase field model

We develop an anisotropic electro chemo mechanical phase field model for NaFPO. The system free energy of some subdomain of volume V is expressed by

$$\Psi(c, \text{grad } c, \epsilon) = \int_B (\psi^h(c) + \psi^{gd}(\text{grad } c) + \psi^e(c, \epsilon)) dV, \quad (9)$$

where ψ^h is the homogeneous Helmholtz free energy density that defines the respective phases, which is constructed in the form

$$\psi^h = k_B T_{ref} N_A c_{max} \left(\bar{\mu}^0 \bar{c} + \frac{T}{T_{ref}} (\bar{c} \ln \bar{c} + (1 - \bar{c}) \ln(1 - \bar{c})) + \bar{c}(1 - \bar{c}) \sum_{i=1}^n \alpha_i (1 - 2\bar{c})^{i-1} \right). \quad (10)$$

Here, \bar{c} is the normalized sodium concentration scaled with the maximum concentration c_{max} as $\bar{c} = c/c_{max}$. N_A , T_{ref} , and k_B are the Avogadro constant, reference temperature, and Boltzmann constant, respectively. The first term on the right hand side of Eq. (10) is the reference chemical potential [1,53,54], and the terms related to T denote the entropy of mixing. We use the Redlich Kister equation [55] to describe the enthalpic effect. The coefficients α_i represent the weight of enthalpy. Later the unknown parameters above will be determined by fitting the DFT based open circuit voltage to capture the two phase segregation between FePO_4 and $\text{Na}_{2/3}\text{FePO}_4$, as well as the single phase region. The gradient energy density

$$\psi^{gd} = k_B T_{ref} N_A c_{max} \left(\frac{1}{2} \lambda |\text{grad } \bar{c}|^2 \right) \quad (11)$$

leads to a diffuse interface between phases with λ being a material constant with units of length squared. The elastic strain energy density ψ^e is given by

$$\psi^e = \frac{1}{2} \epsilon^e : \mathbf{C}(\bar{c}) : \epsilon^e. \quad (12)$$

Here we account for anisotropic elasticity. The rank 4 orthotropic elasticity tensor \mathbf{C} is assumed to be concentration dependent in the form

$$\mathbf{C}(\bar{c}) = (1 - \bar{c}) \mathbf{C}_{\text{FePO}_4} + \bar{c} \mathbf{C}_{\text{NaFePO}_4}, \quad (13)$$

which is a linear interpolation between $\mathbf{C}_{\text{FePO}_4}$ and $\mathbf{C}_{\text{NaFePO}_4}$, the elasticity tensors for FePO_4 and NaFePO_4 , respectively. The elastic strain tensor ϵ^e is expressed by

$$\epsilon^e = \epsilon - \epsilon^s, \quad (14)$$

where ϵ is the total strain tensor

$$\epsilon_{ij} = \frac{1}{2} (u_{i,j} + u_{j,i}) \quad (15)$$

with u_i being the displacement vector. ϵ^s is the concentration dependent stress free strain, which is given by

$$\epsilon^s = \bar{c} \epsilon^0, \quad (16)$$

where ϵ^0 is the anisotropic misfit strain.

The stress can be obtained from the free energy density as [56]

$$\mathbf{T} = \frac{\partial \Psi(c, \text{grad } c, \epsilon)}{\partial \epsilon} = \mathbf{C} : (\epsilon - \bar{c} \epsilon^0). \quad (17)$$

The driving force for diffusion is obtained from carrying out the variation $\delta \Psi(c, \text{grad } c, \epsilon)$ with respect to the sodium concentration giving

$$\begin{aligned} \delta \Psi(c, \text{grad } c, \epsilon) = & \int_B dV \left(\frac{\partial \psi^{mwp}}{\partial c} - k_B T_{ref} N_A \lambda \text{div}(\text{grad } \bar{c}) - \frac{1}{c_{max}} \epsilon^0 : \mathbf{T} \right. \\ & \left. + \frac{1}{2c_{max}} \epsilon^e : (\mathbf{C}_{\text{NaFePO}_4} - \mathbf{C}_{\text{FePO}_4}) : \epsilon^e \right) \delta c \\ & + \int_{\partial B} dA \frac{k_B T_{ref} N_A}{c_{max}} \lambda \text{grad } c \cdot \vec{n} \delta c. \end{aligned} \quad (18)$$

Eq. (18) yields the natural boundary condition on the entire boundary ∂B as

$$\text{grad } c \cdot \vec{n} = 0, \quad (19)$$

which enforces that the interface between phases intersects the particle surface perpendicularly [1]. Thus, the chemical potential is defined as

the variational derivative of the total free energy with respect to the sodium concentration

$$\begin{aligned}\mu &= \frac{\delta \Psi}{\delta c} \\ &= \frac{\partial \Psi^{mwp}}{\partial c} - k_B T_{ref} N_A \lambda \operatorname{div}(\operatorname{grad} \bar{c}) - \frac{1}{c_{max}} \boldsymbol{\epsilon}^0 : \mathbf{T} \\ &\quad + \frac{1}{2c_{max}} \boldsymbol{\epsilon}^e : (\mathbf{C}_{\text{NaFePO}_4} - \mathbf{C}_{\text{FePO}_4}) : \boldsymbol{\epsilon}^e.\end{aligned}\quad (20)$$

It should be noticed that the last term on the right hand side of Eq. (20) is induced by the concentration dependence of elasticity tensor \mathbf{C} .

The mass flux is defined as the amount of Na per reference volume flowing with a certain velocity of Na atoms \vec{v}_{Na}

$$\vec{J} = c \vec{v}_{\text{Na}} = -c \mathbf{M} \cdot \operatorname{grad} \mu, \quad (21)$$

where the gradient of the chemical potential leads to the development of the velocity field. A non negative definite mobility tensor \mathbf{M} is chosen according to

$$\mathbf{M}(c) = \frac{c_{max} - c}{k_B T_{ref} N_A c_{max}} \mathbf{B}, \quad (22)$$

which decreases with increasing lattice site occupancy. The diffusivity tensor is diagonal, $B_{ij} = D_i \delta_{ij}$. Similar to olivine LiFePO_4 [4], defect free olivine NaFePO_4 also exhibits a 1D diffusion channel along (010). It should be noticed that both modeling [57] and experiment [58,59] shows that antisite defects can enhance isotropy of the diffusion in olivine LiFePO_4 .

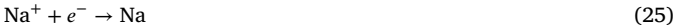
Finally, the balances of mass and linear momentum, respectively, lead to the field equations

$$\frac{\partial c}{\partial t} = \operatorname{div}(c \mathbf{M}(c) \operatorname{grad} \mu), \quad (23)$$

$$\operatorname{div} \mathbf{T} = \vec{0}. \quad (24)$$

Eq. (23) is the mechanically coupled diffusion equation, while Eq. (24) represents mechanical equilibrium. The field equations need to be solved for given initial and boundary conditions.

The electrochemical reaction



takes place at the interface between electrode and electrolyte, and the reaction rate is qualified by the phenomenological Butler Volmer equation [60–62], which relates the current density i to surface over potential η at the interface between electrode and electrolyte as

$$i = i_0 \left[\exp \left((1 - \beta) \frac{F \eta}{k_B T_{ref} N_A} \right) - \exp \left(-\beta \frac{F \eta}{k_B T_{ref} N_A} \right) \right], \quad (26)$$

where i_0 is the exchange current density

$$i_0 = k_0 F (1 - \bar{c}) \exp \left(\frac{(1 - \beta) \mu_+}{k_B T_{ref} N_A} \right) \exp \left(\frac{\beta \mu}{k_B T_{ref} N_A} \right) \quad (27)$$

with k_0 is the reaction rate constant with the unit of $\text{mol}/\text{m}^2 \text{ s}$. The electron transfer symmetry factor is denoted with β , and F is the Faraday constant. Since the species moves in the electrolyte much faster than in the active host material, the chemical potential in the electrolyte μ_+ is set to be zero for simplicity [60]. The surface overpotential η is defined as

$$\eta = \Delta \phi - \frac{\mu_+ - \mu}{F} = \Delta \phi + \frac{\mu}{F}, \quad (28)$$

where $\Delta \phi$ is the voltage drop across interface between electrode and electrolyte, which provides the driving force for Na insertion/extraction and phase changes. We now combine Eqs. (26)–(28) to obtain the Na flux at the interface between electrode and electrolyte as

$$\mathbf{J} = -\frac{i}{F} = k_0 (1 - \bar{c}) \left[\exp \left(-\beta \frac{F \Delta \phi}{k_B T_{ref} N_A} \right) - \exp \left(\frac{\mu + (1 - \beta) F \Delta \phi}{k_B T_{ref} N_A} \right) \right]. \quad (29)$$

It is crucial that through Eqs. (20) and (29) not only the Na concentration, but also its Laplacian (via the gradient energy) and the anisotropies of elasticity and deformation (via the elastic strain energy) contribute to the reaction rate. For the anisotropic diffusion case, the [010] particle surfaces are taken to be in contact with the electrolyte with the Na flux given by Eq. (29), and no flux is applied to other particle surfaces. On the other hand, the Na flux is imposed according to Eq. (29) on all surfaces for the isotropic diffusion case.

The particle is traction free at the surfaces:

$$\mathbf{T} \cdot \vec{n} = \vec{0}. \quad (30)$$

2.2. Material parameters and implementation

2.2.1. The calculated open circuit voltage

Fig. 1a shows the open circuit voltage estimated from DFT calculations (for a description of the calculation of the open circuit voltage by DFT see [63]). All calculations are based on relaxed states. We fit the open circuit voltage to the calculated data with respect to the unknown parameters of the homogeneous Helmholtz free energy density (10), see Fig. 1a. We obtain a good fit with the calculated open circuit voltage curve with $n = 3$, $\bar{\mu}^0 = -113.23$, $\alpha_1 = 1.018$, $\alpha_2 = 3.501$, and $\alpha_3 = -0.792$, in particular at higher concentrations. The deviation at low concentration might be attributed to inhomogeneities in the experimental samples. The fitting results are consistent with those in [41] obtained by fitting to the experimental open circuit voltage curve. For the detailed fitting method, please refer to the Supporting Information. As a result, the dimensionless Landau free energy density [53,54]

$$\bar{\psi}^{mwp} = \frac{\Psi^{mwp}}{k_B T_{ref} N_A c_{max}} = \bar{\psi}^h(\bar{c}) - \frac{\partial \bar{\psi}^h(0.666)}{\partial \bar{c}} \bar{c} = \bar{\psi}^h(\bar{c}) + 114.25 \bar{c} \quad (31)$$

shows a doublewell structure with two different relative minima at $\bar{c} = 0.01$ and $\bar{c} = 0.666$, characterizing the low concentration phase FePO_4 and the high concentration phase $\text{Na}_{2/3}\text{FePO}_4$, respectively, see Fig. 1b. Any terms in the free energy density are normalized according to $\bar{\psi} = \psi / (k_B T_{ref} N_A c_{max})$. The single phase region is represented by the convex shape ($2/3 < \bar{c} < 1$) of the multiwell potential.

2.2.2. The calculated elastic properties

The lattice parameters and elastic constants obtained from GGA and GGA+U calculations are shown in Table 1. To properly describe the electronic and structural properties of FePO_4 and NaFePO_4 , which tend to be Mott insulators, while GGA calculations predict them often to be metals, the Hubbard U correction has been applied. The U correction shows a negligible effect on the lattice constants and increases the cell volume for NaFePO_4 , while for FePO_4 , it is decreased. However, a significant difference in some elastic constants such as c_{22} , c_{12} , and c_{23} has been obtained between the GGA and GGA+U. Eliminating the FeO_6 octahedral distortions caused by using GGA functional and delocalizing the Fe 3d electrons changes the elastic constants compared to GGA+U. The calculated lattice parameters are slightly larger than experimental values determined by Rietveld refinements of the XRD pattern [23], and all the lattice constants a, b, and c increase when sodium is inserted into FePO_4 which is consistent with experimental measurements [23].

The elastic constants c_{11} and c_{44} are larger for FePO_4 than for NaFePO_4 , although FePO_4 is softer. See the Supporting Information for a detailed discussion of this phenomenon. The constants c_{11} (c_{22}) of FePO_4 (NaFePO_4) are obviously larger than other elastic constants, leading to a pronounced elastic anisotropy. The calculated bulk, Young's, and shear moduli, based on the approximations by Voigt, Reuss and Hill's empirical averages are listed in Table 2. It is found that, NaFePO_4 exhibits smaller values for bulk, shear, and Young's moduli than those of LiFePO_4 calculated by Maxisch and Ceder [5].

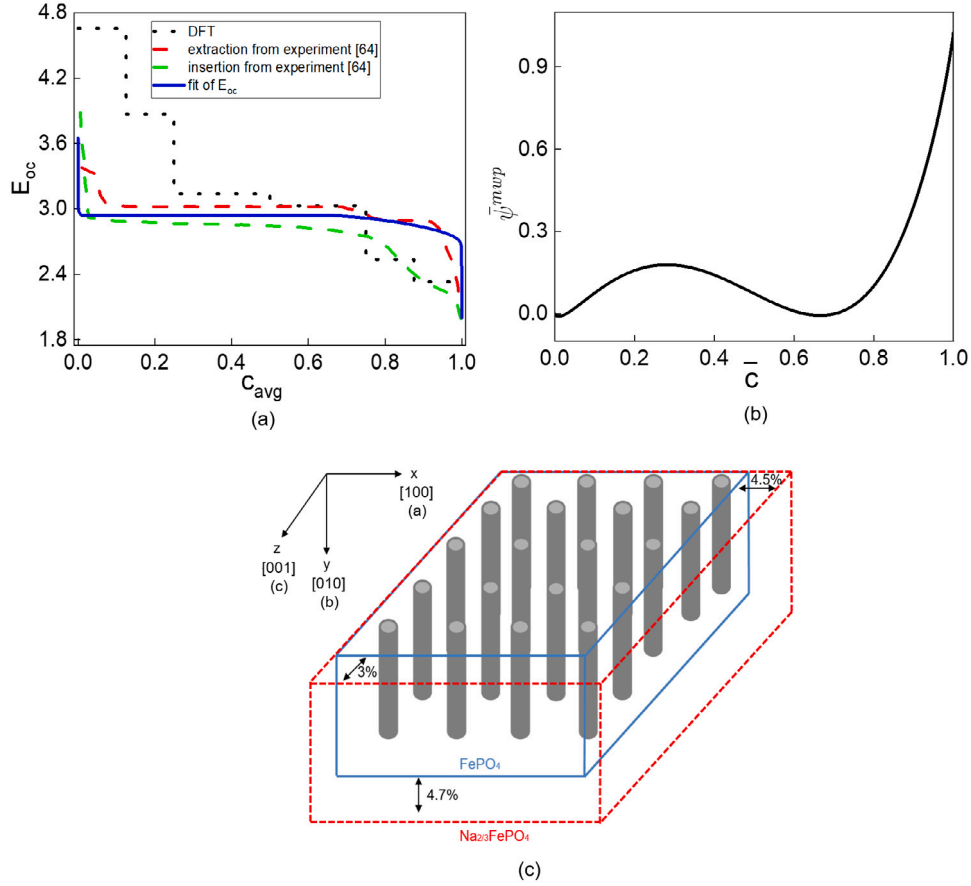


Fig. 1. (a) Voltage profiles estimated from our DFT calculations and experiment [64], and fit of the open-circuit voltage to the calculated data. (b) The multiwell potential of NaFePO. (c) Schematics of prismatic-like single-crystalline particles of NaFePO with 1D Na diffusion channels along (010) and anisotropic misfit strain between FePO₄ and Na_{2/3}FePO₄. Channels are stacked in layers parallel to the yz plane. For each direction, the corresponding Miller index and space group $Pnma$ axis are shown in parentheses.

Table 1

The calculated lattice parameters (given in Å) and elastic constants (given in GPa) of FePO₄ and NaFePO₄ compounds.

	FePO ₄ GGA	FePO ₄ GGA+U	NaFePO ₄ GGA	NaFePO ₄ GGA+U
a [Å]	9.947	9.964	10.453	10.553
b [Å]	5.945	5.889	6.256	6.268
c [Å]	4.890	4.868	5.014	5.014
V [Å ³]	289.20	285.67	327.93	331.66
c_{11}	162.4	179.4	75.3	104.2
c_{22}	111.7	152.8	213.6	172.3
c_{33}	139.0	142.7	112.4	144.2
c_{44}	45.2	51.9	54.2	47.7
c_{55}	28.6	35.7	6.8	31.2
c_{66}	38.2	42.1	44.1	45.2
c_{12}	18.4	33.8	26.2	69.1
c_{13}	66.4	68.3	82.4	83.5
c_{23}	18.0	27.0	10.6	60.6
ρ [g/cm ³]	3.51	3.47	3.45	3.49

Table 2

The calculated polycrystalline bulk, Young, and shear modulus in GPa, as well as the Poisson ratio obtained with GGA+U.

Averaging scheme	Bulk modulus	Young's modulus	Shear modulus	Poisson's ratio
FePO₄				
Voigt	$K_V = 81.45$	$E_V = 122.46$	$G_V = 49.00$	$\nu_V = 0.2494$
Reuss	$K_R = 79.30$	$E_R = 116.56$	$G_R = 46.44$	$\nu_R = 0.2550$
Hill	$K_H = 80.37$	$E_H = 119.51$	$G_H = 47.72$	$\nu_H = 0.2522$
NaFePO₄				
Voigt	$K_V = 94.13$	$E_V = 101.99$	$G_V = 38.65$	$\nu_V = 0.3194$
Reuss	$K_R = 91.45$	$E_R = 88.49$	$G_R = 33.05$	$\nu_R = 0.3387$
Hill	$K_H = 92.79$	$E_H = 95.28$	$G_H = 35.85$	$\nu_H = 0.3289$

2.3. Implementation

Fig. 1c shows the schematic of a prismatic like single crystalline particle of NaFePO with 1D Na diffusion channels along (010) and anisotropic misfit strain between FePO₄ and Na_{2/3}FePO₄ [23]. Consideration of the two phase region shows that, the a , b and c axes increase by 4.5, 4.7 and 3.0%, respectively, for Na _{x} FePO₄ ($x = 0$ to 2/3) but by 5.1, 3.6 and -1.9% [65], respectively, for Li _{x} FePO₄ ($x = 0$ to 1). Thus NaFePO exhibits a more isotropic expansion than its lithium counterpart. For the purpose of achieving representative

statements, in our simulations we consider a full 3D single crystalline particle with cubic morphology of size $L = 500$ nm. A voltage drop $\Delta\phi = -50$ mV is applied to provide a driving force for Na insertion into particles. The electron transfer symmetry factor β is set to 0.5. The material parameters for NaFePO are summarized in Table 3. The average concentration c_{avg} , also called ‘‘state of charge’’ (SOC), is defined as $c_{avg} = \int_B \bar{c} dV / V$, and $\bar{\psi}_{avg} = \int_B \bar{\psi} dV / V$ is the dimensionless average system free energy, see also Eq. (9).

Since the diffusion equation (23) involves fourth order spatial derivatives in concentration and third order spatial derivatives in displacement, the standard finite element method with C^0 continuous Lagrange basis functions is not sufficient for discretization. To overcome this numerical difficulty, we introduce the chemical potential as an additional degree of freedom to split this fourth order partial differential equation into two second order equations. This coupled system

Table 3

The material parameters for NaFPO.

Parameters	Values
$\bar{\mu}^0$	-113.23
α_1	1.018
α_2	3.501
α_3	-0.792
λ	1.8×10^{-17} (m ²) [38]
D	1×10^{-15} (m ² /s) [38]
c_{max}	2.1×10^4 (mol/m ³) [38]
ϵ^0	$\begin{pmatrix} 4.5\% & 0 & 0 \\ 0 & 4.7\% & 0 \\ 0 & 0 & 3\% \end{pmatrix}$ [23]
C_{FePO_4}	$\begin{pmatrix} 179.4 & 33.8 & 68.3 & 0 & 0 & 0 \\ 33.8 & 152.8 & 27.0 & 0 & 0 & 0 \\ 68.3 & 27.0 & 142.7 & 0 & 0 & 0 \\ 0 & 0 & 0 & 51.9 & 0 & 0 \\ 0 & 0 & 0 & 0 & 35.7 & 0 \\ 0 & 0 & 0 & 0 & 0 & 42.1 \end{pmatrix}$ (GPa)
C_{NaFePO_4}	$\begin{pmatrix} 104.2 & 69.1 & 83.5 & 0 & 0 & 0 \\ 69.1 & 172.3 & 60.6 & 0 & 0 & 0 \\ 83.5 & 60.6 & 144.2 & 0 & 0 & 0 \\ 0 & 0 & 0 & 47.7 & 0 & 0 \\ 0 & 0 & 0 & 0 & 31.2 & 0 \\ 0 & 0 & 0 & 0 & 0 & 45.2 \end{pmatrix}$ (GPa)

Table 4

Four regimes of phase-separating dynamics.

Parameters	Formulations	Notes
Isotropic SRL	$Da_{11} = Da_{22} = Da_{33} = 3.47 \times 10^{-5}$	$D_{11} = D_{22} = D_{33} = D$
Isotropic BDL	$Da_{11} = Da_{22} = Da_{33} = 7$	$D_{11} = D_{22} = D_{33} = D$
Anisotropic SRL	$Da_{22} = 3.47 \times 10^{-5}$	$D_{11} = D_{33} = 0, D_{22} = D$
Anisotropic BDL	$Da_{22} = 7$	$D_{11} = D_{33} = 0, D_{22} = D$

is described by the three Eqs. (20), (23), and (24) with the independent variables c , μ , and \bar{u} , respectively. The resulting set of equations is first written in weak form (see the Supporting Information), and then implemented in the finite element, multiphysics framework MOOSE [66]. 3 D simulations are run on 224, 448 or 1008 processors and take up to a maximum of 13 days. For more detailed numerical methods, please refer to the Supporting Information.

3. Results and discussion

3.1. 3D microstructure evolution

In order to investigate the influence of kinetic competition between surface reactions and bulk diffusion on microstructure evolution during sodium insertion, the Damköhler number

$$Da_{ii} = \frac{k_0 L}{c_{max} D_{ii}} \quad (32)$$

is introduced which compares reaction and diffusion time scales. Consistent with the definition of Da_{ii} , we will study four different regimes of phase separating dynamics, including isotropic surface reaction limited (SRL) dynamics, isotropic bulk diffusion limited (BDL) dynamics, anisotropic SRL dynamics, and anisotropic BDL dynamics, as summarized in Table 4.

3.1.1. Isotropic surface reaction limited dynamics

First, we focus on the isotropic SRL regime where surface reactions are slower than bulk diffusion in all directions. Fig. 2 shows the system free energy evolution of NaFPO by the solid line, while the evolution of the 3D microstructure and the corresponding maximum principal stress, σ_I , is shown in Fig. 3. For comparison purposes, the dimensionless multiwell potential versus normalized concentration is also entered in Fig. 2. The solid line coinciding with the normalized multiwell potential curve corresponds to homogeneous states whereas the solid line nearby the path of the Maxwell construction connecting the neighborhoods of

the two minima by a common tangent indicates phase segregated states. Interestingly, the curve of the system free energy exhibits five ‘‘kinks’’ (A E) in the form of a sharp dropping process of the system free energy. What is the physical behavior underlying these ‘‘kinks’’? The insertion process initially takes place through an almost homogeneous filling throughout the particle. Once c_{avg} gets close to 7.266%, the high concentration phase $Na_{2/3}FePO_4$ first nucleates at the particle corners. The initiation of phase nucleation manifests itself macroscopically through the first ‘‘kink’’ A in the system free energy curve shown in Fig. 2. In a short nucleation period, more sodium rich islands quickly form along the particle edges (see $c_{avg} = 7.27\%$), and then the four sodium rich islands at the [001] edges coalesce into two individual sodium rich domains at particle corners, while the sodium rich islands at the center of the [100] edges shrink and disappear (see $c_{avg} = 7.291\%$), leading to a decrease in the number of individual sodium rich islands and thus the minimization of the total system free energy. The stresses are mainly focused at the interface between the low concentration phase $FePO_4$ and the intermediate phase $Na_{2/3}FePO_4$. As insertion proceeds, when c_{avg} approaching 9.521%, the smaller $Na_{2/3}FePO_4$ nuclei at particle corners disappear, and the larger one expands quickly along [001] but shows much slower expansion in other directions, corresponding to the second ‘‘kink’’ B shown in Fig. 2. Such expansion anisotropy can be attributed to the anisotropic misfit strain between $FePO_4$ and $Na_{2/3}FePO_4$, which is smallest along [001] (3%) but along [100] is 4.5% and along [010] is 4.7%. Thus the elastic strain energy supports preferential phase expansion along [001] to reduce stresses at the interface.

After an initial fast expansion along [001], when c_{avg} approaching 29.24%, a quasi equilibrium intercalation wave is formed, corresponding to the third ‘‘kink’’ C shown in Fig. 2. During the single wave propagation period, the phase boundary between $FePO_4$ and $Na_{2/3}FePO_4$ moves along [100], and has a curved shape instead of a flat interface perfectly aligned with [010], and it changes from convex to concave. Near the particle surface, in the absence of surface wetting, the phase boundary bends and is perpendicular to each particle side. This growth direction along [100] agrees well with the experimental observation of LiFPO [26,28].

The filling of Na ions proceeds through the motion of this phase boundary until the intercalation wave reaches the other [100] facet, corresponding to the fourth ‘‘kink’’ D shown in Fig. 2. The minimization of the total system free energy leads to the abrupt appearance of a sodium poor cylindrical island along [001], see $c_{avg} = 54.843\%$. When c_{avg} grows to 61.239%, the sodium poor island shrinks into an intricate phase morphology with a ‘‘singular point’’, and then the intermediate phase $Na_{2/3}FePO_4$ quickly occupies all of the particle, corresponding to the fifth ‘‘kink’’ E shown in Fig. 2. In the single phase region, the insertion process occurs through the formation of a solid solution Na_xFePO_4 , leading to an almost homogeneous state. It should be noticed that the single phase region is almost stress free due to the sluggish Na surface insertion kinetics such that almost no gradient in Na distribution occurs.

3.1.2. Isotropic bulk diffusion limited dynamics

When bulk diffusion in all directions is much slower than surface reactions, a shrinking core morphology is formed in the isotropic BDL regime as shown in Fig. 4. Na atoms start accumulating at the corners of the particle, and quickly pile up at the edges of the particle, see $c_{avg} = 4\%$, since the inserted Na atoms do not have enough time to diffuse inside the particle. At later times, the nuclei at the edges of the particle coarsen to form a core shell structure, in which the sodium rich phase occupies the shell of the particle while the sodium poor one is situated in its core. The core shape appears first that of the geometry of the particle, and then develops to spherical in order to minimize the area of the interface. In contrast to the isotropic SRL regime, in the single phase region stresses still exist due to the concentration gradient in the particle, see $c_{avg} = 80.123\%$.

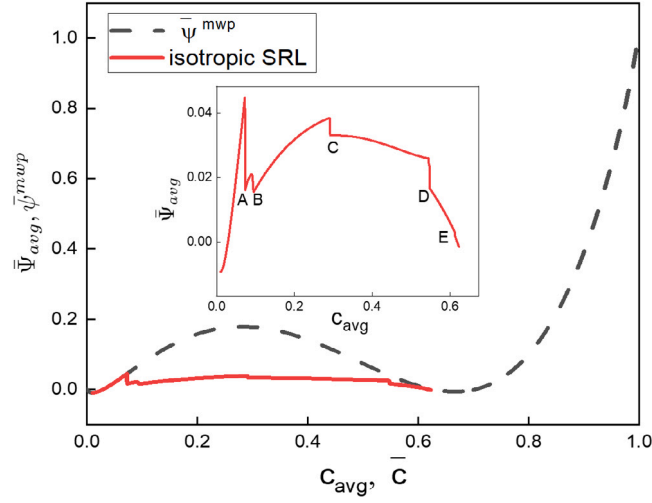


Fig. 2. Normalized average system free energy $\bar{\Psi}_{avg}$ and, for comparison, normalized multiwell potential $\bar{\psi}^{mwp}$ as function of c_{avg} and \bar{c} , respectively.

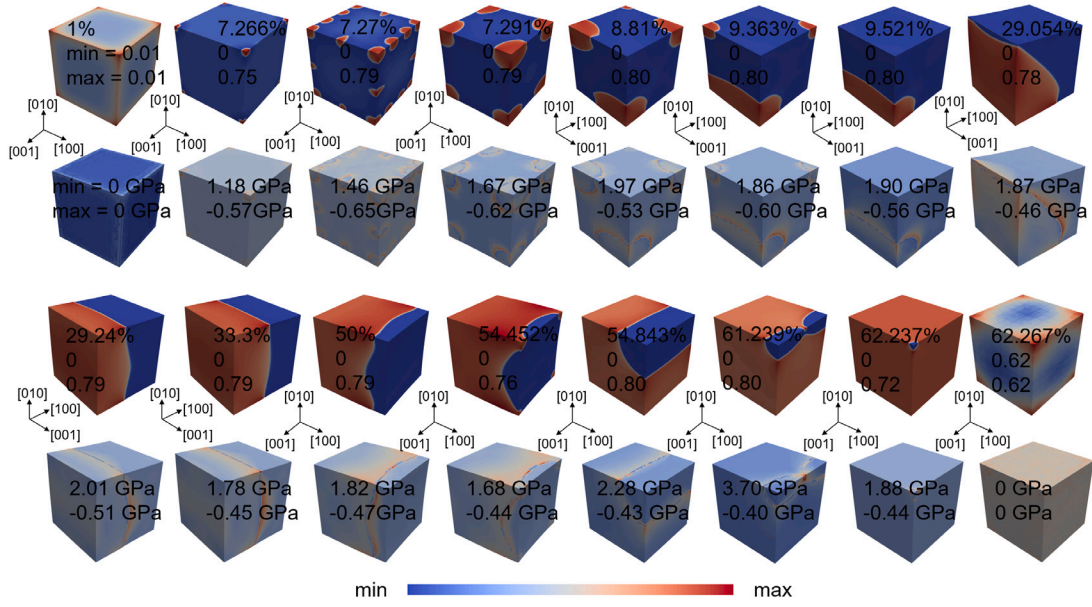


Fig. 3. Evolution of the 3D microstructure and the corresponding maximum principal stress σ_1 as functions of c_{avg} during sodium insertion for the isotropic SRL regime.

3.1.3. Anisotropic surface reaction limited dynamics

How do the microstructure of the phase separation and the stresses evolve when Na moves rapidly along the [010] migration channels but has negligible diffusivity in other directions? We first study the anisotropic SRL regime where surface reactions are much slower than Na diffusion in the [010] direction but Na diffusion in the [100] and [001] directions is negligible. Fig. 5 shows the evolution of the 3D microstructure and the corresponding maximum principal stress σ_1 . The system is in a homogeneous state at the beginning of sodium insertion. Once c_{avg} gets close to around 6.03%, which is a little bit earlier than for isotropic SRL, sodium rich islands first nucleate around particle corners of the [010] surfaces, and then the $\text{Na}_{2/3}\text{FePO}_4$ nuclei develop quickly along [001] but exhibit much slower expansion in other directions in the [010] surfaces. Similar to the isotropic SRL regime, such expansion anisotropy comes from the anisotropic misfit strain. When c_{avg} approaches 9.692%, which is much earlier than in the isotropic SRL regime, NaFPO displays the dynamics of single wave propagation along [010]. During the single wave propagation period, the phase boundary shows nearly a flat morphology instead of the curved interface of the isotropic SRL regime. This is attributed to

the 1D diffusion channel along [010] such that the intercalation wave uniformly moves along [010]. The phase boundary thus moves in such a way that it is perpendicular to each channel.

The filling of Na ions proceeds through the motion of this phase boundary until the intercalation wave reaches the top [010] facet. When c_{avg} approaches 57.157%, an intricate phase morphology is formed with a “singular point”, and then the phase segregated state quickly shifts into the homogeneous state. Similar to the isotropic SRL regime, the single phase region is almost stress free due to the absence of any concentration gradients.

3.1.4. Anisotropic bulk diffusion limited dynamics

When Na diffusion in [010] direction is much slower than surface reactions but Na diffusion in the [100] and [001] directions is negligible, the shrinking core structure is not formed in the anisotropic BDL regime. Both the shape of the interface morphology and the diffusive dynamics are altered by the anisotropic diffusion, as shown in Fig. 6. At the beginning of insertion Na atoms quickly pile up at the complete top and bottom surfaces since the inserted Na atoms do not have enough time to diffuse inside the particle along [010]. NaFPO then

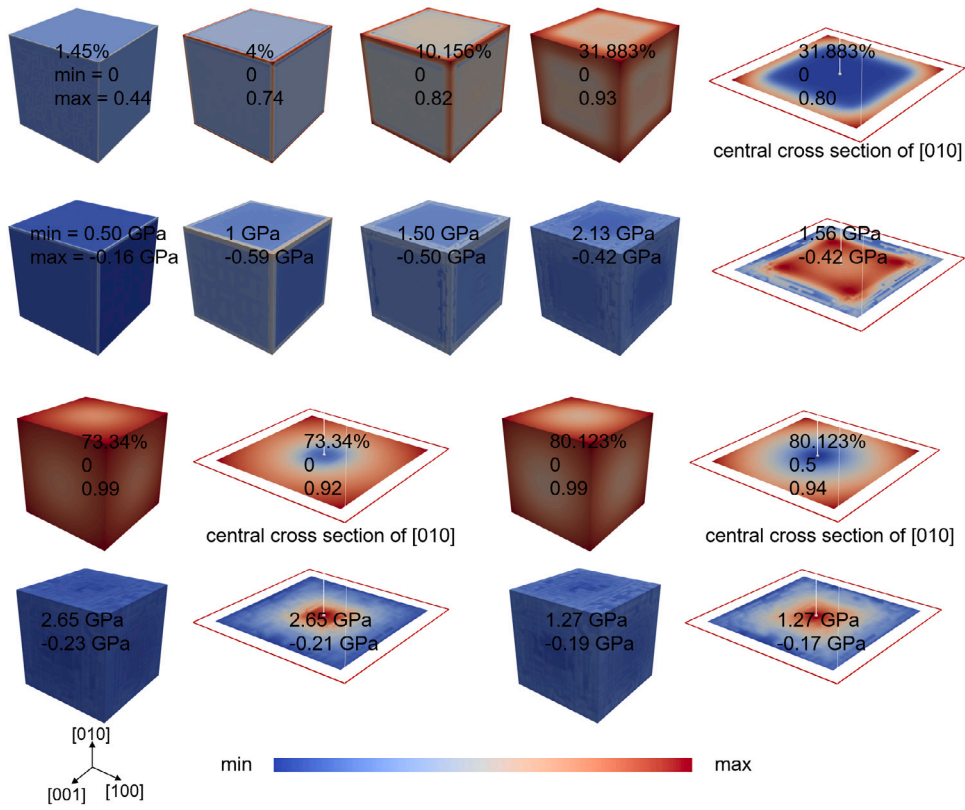


Fig. 4. Evolution of the 3D microstructure and the corresponding maximum principal stress σ_1 as functions of c_{avg} during sodium insertion for the isotropic BDL regime.

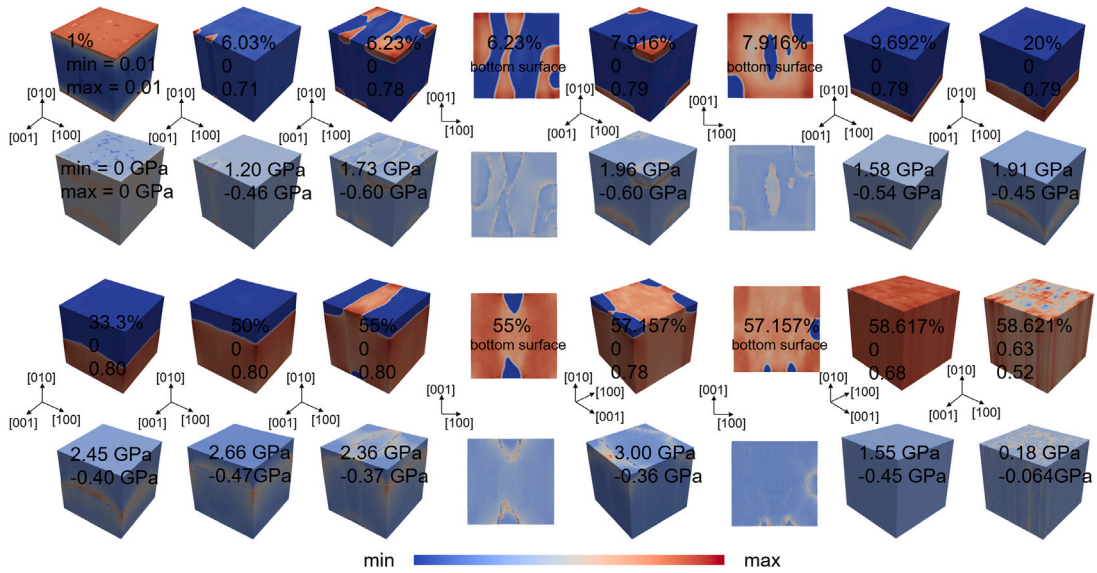


Fig. 5. Evolution of the 3D microstructure and the corresponding maximum principal stress σ_1 as functions of c_{avg} during sodium insertion for the anisotropic SRL regime.

displays the dynamics of double wave propagation: the two sodium rich islands at the [010] surfaces gradually grow along [010], and the phase boundaries always go all the way across the particle. When c_{avg} approaches 67.059%, the two sodium rich domains not only meet each other at the [001] surfaces but also coalesce inside the particle into an hourglass like sodium rich domain. This is due to the fact that the Na atoms are confined to 1D diffusion channels along [010]. As insertion proceeds, this hourglass like sodium rich domain gradually expands at the expense of the sodium poor domain around it. At the end of phase segregation just before the system enters the single phase

region, small sodium poor islands remain located at each [010] side, see $c_{avg} = 85.347\%$. Similar to the isotropic BDL regime, in the single phase region stresses still exist due to the concentration gradient in the particle.

3.1.5. Comparison of four dynamic regimes

In contrast to the intercalation waves, including single wave propagation and double wave propagation, the core shell structure of NaFPO is extremely energetically unfavorable, which can be verified by the plot of the system free energy shown in Fig. 7a. Here, the system free

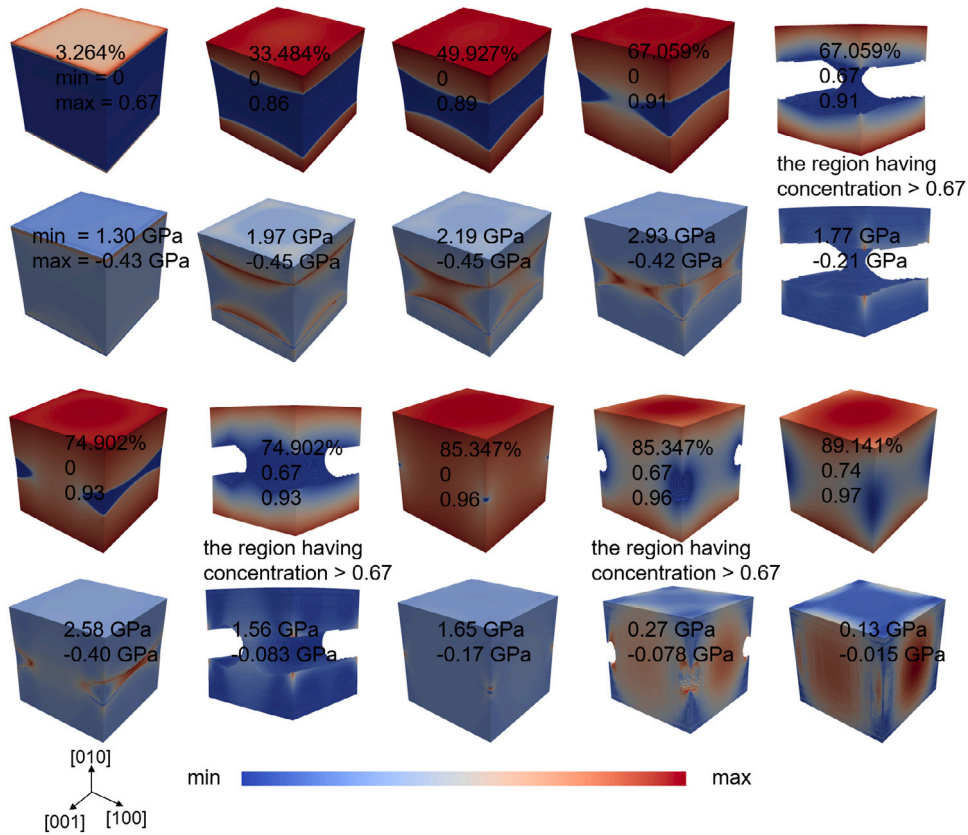


Fig. 6. Evolution of the 3D microstructure and the corresponding maximum principal stress σ_I as functions of c_{avg} during sodium insertion for the anisotropic BDL regime.

energy from the core shell structure is even above the dimensionless multiwell potential. Furthermore, single wave propagation along [010] is more energetically expensive than that along [100], even though the latter has a larger interface area due to its curvature. This is related to the anisotropy of deformation and elasticity, which will be discussed later.

The maximum solubility limit is over 2/3 within two phase coexistence even in the SRL regimes, see Fig. 7b, which matches the experimental observation based on Rietveld refinements of synchrotron operando XRD data [67]. This is related to stress assisted diffusion in the sodium rich phase [41]. As expected, the maximum solubility limits at the phase segregated states are always bigger in the BDL regimes compared to the SRL regimes, and a maximum miscibility gap is achieved in the isotropic BDL regime.

Now we focus on the stresses in a NaFePO particle during the insertion process for these four dynamic regimes, as shown in Fig. 7c. For the SRL regimes, the maximum compressive stress magnitude is reached when phase nucleation is initiated, and the maximum tensile stress is reached at the end of phase segregation just before the system enters the single phase region. For example, the maximum tensile stress is located at the “singular point” of the intricate phase morphology, see $c_{avg} = 61.239\%$ of Fig. 3 and $c_{avg} = 57.157\%$ of Fig. 5, respectively, for the isotropic and anisotropic SRL regimes. Similar to the SRL regimes, the maximum tensile stress in the core shell structure is reached at the end of phase segregation just before the system enters the single phase region, which is located at the center of the particle, see $c_{avg} = 73.34\%$ of Fig. 4. Among these four dynamic regimes, the overall stress levels over a larger period of insertion in the whole particle of NaFePO are higher in the anisotropic diffusion cases, especially for the double wave propagation structure, although a peak of the stresses at the phase segregated states is achieved in the structure of single wave propagation along [100]. This indicates that the phase morphology of the double wave propagation is more prone to particle cracking and mechanical

degradation, and the isotropic mobility of Na induces a stress reduction behavior.

3.2. Influence of the anisotropy of misfit strain and elasticity

One notable aspect of microstructure evolution is that NaFePO displays the dynamics of single wave propagation along [100] in the isotropic SRL regime. But why does the phase boundary not move along the other directions despite insertion taking place equally at all particle surfaces? We find that phase boundary motion along [100] is thermodynamically limited by minimization of the elastic strain energy, which is controlled by the competition between the anisotropic misfit strain and the concentration dependent anisotropic elasticity tensor as will be discussed now.

The anisotropic misfit strain favors phase boundary motion along [010] as it will not then introduce a phase boundary plane including the [010] axis along which the misfit strain is largest. This is well verified through a control simulation, in which, we consider the anisotropic misfit strain but an isotropic elasticity tensor, see Fig. 8a. The latter is taken from Hill’s average of Young’s modulus and Poisson’s ratio between FePO_4 and NaFePO_4 . Furthermore, to study the influence of elastic anisotropy, a series of simulations are performed, in which we consider anisotropic elasticity tensors $\mathbf{C}_{\text{FePO}_4}$, $\mathbf{C}_{\text{NaFePO}_4}$, and $\mathbf{C}(\bar{c})$ but an isotropic misfit strain, see Fig. 8b d. We find that the anisotropic elasticity tensor $\mathbf{C}_{\text{FePO}_4}$ favors phase boundary motion along [100], while the anisotropic elasticity tensor $\mathbf{C}_{\text{NaFePO}_4}$ favors phase boundary motion along [001]. Finally, similar to the anisotropic elasticity tensor $\mathbf{C}_{\text{FePO}_4}$, the concentration dependent anisotropic elasticity tensor $\mathbf{C}(\bar{c})$ favors phase boundary motion along [100], since the anisotropic elasticity tensor $\mathbf{C}_{\text{FePO}_4}$ plays a dominant role in the early insertion process.

As a result we conclude that the concentration dependent anisotropic elasticity tensor $\mathbf{C}(\bar{c})$ “wins” the competition with the anisotropic misfit strain to minimize the elastic strain energy, leading

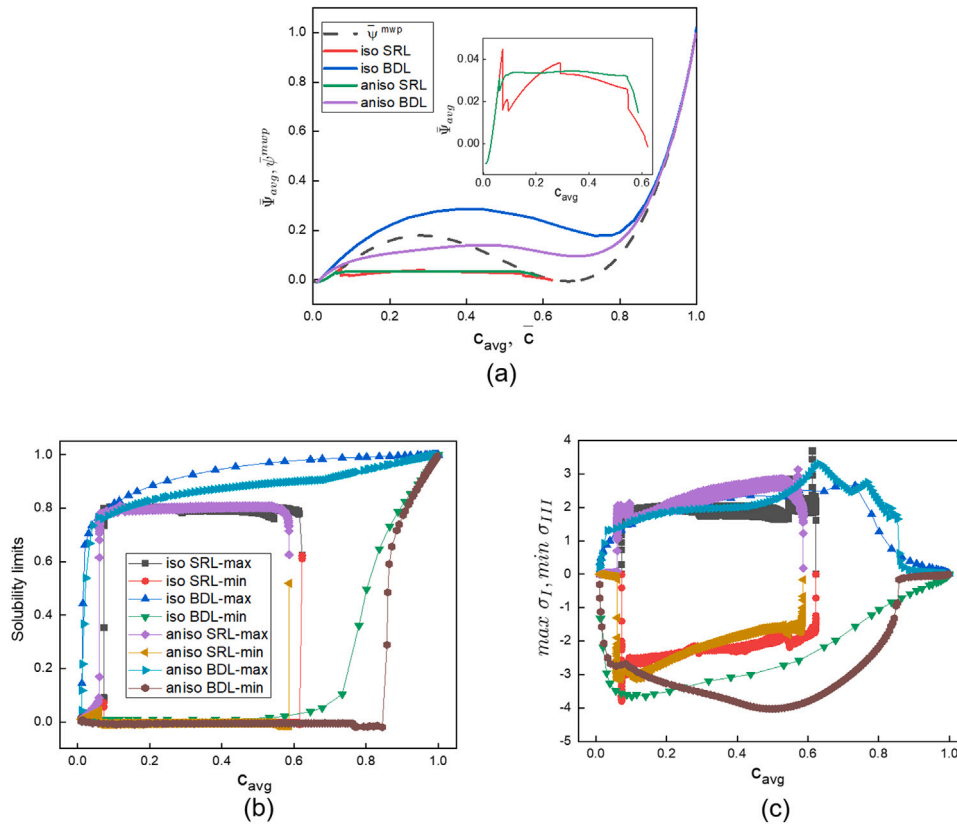


Fig. 7. Comparison of four dynamic regimes. (a) Normalized average system free energy $\bar{\Psi}_{avg}$ and normalized multiwell potential $\bar{\psi}^{mwp}$ as functions of c_{avg} and $\bar{\epsilon}$, respectively. (b) Solubility limits and (c) the highest value of the maximum principal stress $max \sigma_I$ and the lowest value of the minimum principal stress $min \sigma_{III}$ as functions of c_{avg} .

to phase boundary motion along [100]. This is well substantiated through another control simulation, in which we increase the misfit strain along [010] from 4.7% into 6%. It is found that, in this control simulation, the anisotropic misfit strain “wins” this competition to minimize the elastic strain energy, leading to phase boundary motion along [010] (we do not show this result here). Furthermore, if we take the anisotropic elasticity tensor C_{NaFePO_4} into account in our model rather than the concentration dependent anisotropic elasticity tensor $C(\bar{\epsilon})$, the original anisotropic misfit strain “wins” this competition with C_{NaFePO_4} to minimize the elastic strain energy, leading to the phase boundary motion along [010], see Fig. 8e. This is also well supported through a control simulation, in which, we increase the misfit strain along [001] from 3% into 4.45%. This control simulation shows that the anisotropic elasticity tensor C_{NaFePO_4} “wins” this competition to minimize the elastic strain energy, leading to phase boundary motion along [001] (we do not show this result here). This means that the concentration dependence of the anisotropic elasticity tensor plays a nontrivial role in determining the phase boundary orientation. All together, it can be concluded that phase boundary motion of NaFPO is controlled by the concentration dependent anisotropic elasticity tensor and, to a lesser degree, affected by the anisotropic misfit strain.

Another notable aspect of microstructure evolution is that the phase boundary moves along [010] in the anisotropic SRL regime, even although the concentration dependent anisotropic elasticity tensor favors a phase boundary motion along [100]. At first glance it may seem that anisotropic misfit strain “wins” this competition in the anisotropic SRL regime to minimize the elastic strain energy, leading to phase boundary motion in the [010] direction. This is not verified through a control simulation in which we consider a concentration dependent anisotropic elasticity tensor but an isotropic misfit strain. It is found that, in this control simulation, the phase boundary still moves along [010] (we do not show this result here). Indeed, the Na atoms are

strictly confined to 1D diffusion channels along [010], such that the full blocking of the diffusion channels along [100] and [001] leads to a phase boundary motion along [010]. This is well illustrated through a control simulation, in which the diffusion channels along [100] and [001] are not fully blocked ($D_{11} = D_{33} = 0.01D, D_{22} = D$), and the [010] particle surfaces, only, are still taken to be in contact with the electrolyte. It is found that the phase boundary moves along [100] in this control simulation, see Fig. 8f, which matches the isotropic SRL regime. In this case, anisotropic elasticity controls phase boundary motion, even although diffusion along [010] is still much faster than in the other two directions. Therefore, the pure 1D Na diffusion channel plays a more dominant role in phase boundary motion than elasticity, and single wave propagation along [010] is in a kinetically arrested state, rather than the thermodynamically energetic minimum. As a result, as shown in Fig. 7, it is energetically more expensive for single wave propagation to occur along [010] compared to that along [100], even though the latter has a larger curved interface area. A possible way to attain low energy phase boundaries along [100] is via an antisite defects actuated in plane diffusion mechanism where in plane diffusion normal to [010] is activated. Such defect actuated out of 1D diffusion has been verified by both modeling [57] and experiment [58,59] in olivine LiFePO₄. Fig. 8f shows that a small amount of in plane diffusion permits phase evolution into this structure that minimizes the elastic strain energy. However, this mechanism is not possible in defect free olivine NaFPO₄, where only 1D diffusion along a specific crystallographic channel direction is allowed. We suggest that characterization of the orientation of the phase boundary could be a potent way to predict the existence of antisite defects in NaFPO particles.

4. Conclusions

We have established a virtual multiscale modeling chain to construct an anisotropic electro chemo mechanical phase field model

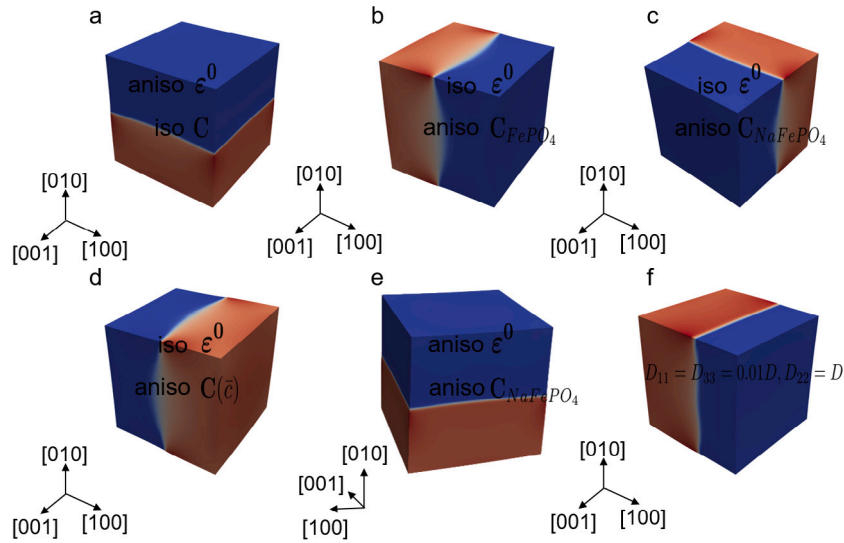


Fig. 8. Effects of the anisotropies of deformation and elasticity. (a) 3D microstructure at $c_{avg} = 0.333$ assuming an anisotropic misfit strain but an isotropic elasticity tensor taken from Hill's average of Young's modulus and Poisson's ratio between FePO_4 and NaFePO_4 . (b–d) 3D microstructure at $c_{avg} = 0.333$ assuming an anisotropic elasticity tensor $C_{\text{FePO}_4}/C_{\text{NaFePO}_4}/C(\bar{\epsilon})$ but an isotropic misfit strain. (e) 3D microstructure at $c_{avg} = 0.333$ assuming an anisotropic elasticity tensor C_{NaFePO_4} and an anisotropic misfit strain. (f) 3D microstructure at $c_{avg} = 0.4$ in the anisotropic SRL regime where the in-plane diffusion is activated ($D_{11} = D_{33} = 0.01D, D_{22} = D$).

based on DFT simulations for NaFPO of NIBs. In this way, the model accounts for phase changes, electrochemical reactions, anisotropic diffusion, anisotropic misfit strain, and anisotropic elasticity, as well as the concentration dependence of the elasticity tensor. First principles calculations show that NaFePO_4 exhibits a pronounced elastic anisotropy with a significantly larger elastic constant c_{22} compared to the other elastic constants, leading to pronounced elastic anisotropy. The multiwell potential of Na_xFePO_4 for the full range of concentration is determined based on the calculated open circuit voltage. We investigate how diffusion kinetics and crystal anisotropy influence 3D microstructure evolution of NaFPO, and capture four different phase separating dynamics.

Our simulations in surface reaction limited regimes predict the generation of a kinetically arrested state of single wave propagation along [010] with a flat interface morphology, which is induced by a 1D Na diffusion channel rather than by competition between the concentration dependent anisotropic elasticity tensor and the anisotropic misfit strain. The low energy phase boundary orientation of single wave propagation along [100] with a curved interface morphology can be obtained by an antisite defects actuated in plane diffusion mechanism, even for a small amount of in plane diffusion. Phase boundary motion along [100] is thermodynamically limited by the minimization of elastic strain energy, which is controlled by the concentration dependent anisotropic elasticity tensor and, to a lesser degree, affected by the anisotropic misfit strain. As for fast surface reactions, in contrast to the classical shrinking core structure from the isotropic diffusion case, double wave propagation along [010] is observed when Na atoms are confined to 1D diffusion channels. We find that the structure of double wave propagation is more prone to particle cracking and mechanical degradation as a result of the higher overall stress level. It is suggested that characterization of the orientation of the phase boundary could be a potent method to predict the existence of antisite defects in NaFPO particles.

More generally, the calculated elastic and electronic properties can provide significant input for the future study of NaFPO (see the Supporting Information for the calculated electronic properties). The virtual multiscale modeling chain, which combines an anisotropic electrochemo mechanical phase field model and DFT calculations, is general and can be adjusted to other phase separating electrode materials for studying 3D microstructure evolution. Beyond NaFPO, we envision

that the virtual multiscale modeling chain may present an opportunity to identify material compositions having desired phase behavior with better mechanical stability and thus better battery performance by defect actuated out of 1D diffusion of an intercalation electrode material.

CRediT authorship contribution statement

Tao Zhang: Conceptualization, Methodology, Software, Formal analysis, Investigation, Data curation, Writing original draft. **Mohsen Sotoudeh:** Methodology, Software, Formal analysis, Investigation, Data curation, Writing original draft. **Axel Groß:** Resources, Writing review & editing, Supervision, Project administration, Funding acquisition. **Robert M. McMeeking:** Writing review & editing, Supervision. **Marc Kamlah:** Conceptualization, Resources, Writing review & editing, Supervision, Project administration, Funding acquisition.

Declaration of competing interest

The authors declare that they have no known competing financial interests or personal relationships that could have appeared to influence the work reported in this paper.

Data availability

Data will be made available on request.

Acknowledgments

This work contributes to the research performed at CELEST (Center for Electrochemical Energy Storage Ulm Karlsruhe) and was funded by the German Research Foundation (DFG) under Project ID 390874152 (POLiS Cluster of Excellence). Further support by the Dr. Barbara Mez Starck Foundation and computer time provided by the state of Baden Württemberg through bwHPC and the German Research Foundation (DFG) through grant no. INST 40/575 1 FUGG (JUSTUS 2 cluster) are gratefully acknowledged. The results presented were partly achieved during a six month visit of Tao Zhang in the group of Professor Robert M. McMeeking at the University of California, Santa Barbara. This research stay was funded by Karlsruhe House of Young Scientists (KHYS).

References

- [1] D.A. Cogswell, M.Z. Bazant, *ACS Nano* 6 (3) (2012) 2215–2225.
- [2] M. Tang, J.F. Belak, M.R. Dorr, *J. Phys. Chem. C* 115 (11) (2011) 4922–4926.
- [3] K. Yang, M. Tang, *J. Mater. Chem. A* 8 (6) (2020) 3060–3070.
- [4] D. Morgan, A. Van der Ven, G. Ceder, *Electrochem. Solid-State Lett.* 7 (2) (2003) A30.
- [5] T. Maxisch, G. Ceder, *Phys. Rev. B* 73 (17) (2006) 174112.
- [6] M. Klinsmann, D. Rosato, M. Kamlah, R.M. McMeeking, *J. Power Sources* 331 (2016) 32–42.
- [7] R. Xu, K. Zhao, *J. Mech. Phys. Solids* 121 (2018) 258–280.
- [8] D. Chen, D. Kramer, R. Mönig, *Electrochim. Acta* 259 (2018) 939–948.
- [9] M. Klinsmann, D. Rosato, M. Kamlah, R.M. McMeeking, *J. Mech. Phys. Solids* 92 (2016) 313–344.
- [10] M. Ganser, F.E. Hildebrand, M. Kamlah, R.M. McMeeking, *J. Mech. Phys. Solids* 125 (2019) 681–713.
- [11] D. Zhang, J. Sheth, B.W. Sheldon, A.R. Balakrishna, *J. Mech. Phys. Solids* 155 (2021) 104551.
- [12] M. Janzen, D. Kramer, R. Mönig, *Energy Technol.* 9 (6) (2021) 2000867.
- [13] D. Bistri, A. Afshar, C.V. Di Leo, *Meccanica* 56 (6) (2021) 1523–1554.
- [14] A.R. Balakrishna, *J. Electrochem. Energy Convers. Storage* 19 (4) (2022) 040802.
- [15] A. Afshar, C.V. Di Leo, *J. Mech. Phys. Solids* 151 (2021) 104368.
- [16] D. Buchholz, A. Moretti, R. Kloepsch, S. Nowak, V. Siozios, M. Winter, S. Passerini, *Chem. Mater.* 25 (2) (2013) 142–148.
- [17] C. Vaalma, D. Buchholz, M. Weil, S. Passerini, *Nat. Rev. Mater.* 3 (4) (2018) 1–11.
- [18] X. Dou, I. Hasa, D. Saurel, C. Vaalma, L. Wu, D. Buchholz, D. Bresser, S. Komaba, S. Passerini, *Mater. Today* 23 (2019) 87–104.
- [19] V. Palomares, P. Serras, I. Villaluenga, K.B. Hueso, J. Carretero-González, T. Rojo, *Energy Environ. Sci.* 5 (3) (2012) 5884–5901.
- [20] P. Moreau, D. Guyomard, J. Gaubicher, F. Boucher, *Chem. Mater.* 22 (14) (2010) 4126–4128.
- [21] N. Yabuuchi, K. Kubota, M. Dahbi, S. Komaba, *Chem. Rev.* 114 (23) (2014) 11636–11682.
- [22] J. Dodd, R. Yazami, B. Fultz, *Electrochem. Solid-State Lett.* 9 (3) (2006) A151–A155.
- [23] J. Lu, S.C. Chung, S.-i. Nishimura, A. Yamada, *Chem. Mater.* 25 (22) (2013) 4557–4565.
- [24] B. Özdogru, H. Dykes, S. Padwal, S. Harimkar, Ö.Ö. Çapraz, *Electrochim. Acta* 353 (2020) 136594.
- [25] B. Özdogru, H. Dykes, D. Gregory, D. Saurel, V. Murugesan, M. Casas-Cabanas, Ö.Ö. Çapraz, *J. Power Sources* 507 (2021) 230297.
- [26] G. Chen, X. Song, T.J. Richardson, *Electrochem. Solid-State Lett.* 9 (6) (2006) A295–A298.
- [27] L. Laffont, C. Delacourt, P. Gibot, M.Y. Wu, P. Kooyman, C. Masquelier, J.M. Tarascon, *Chem. Mater.* 18 (23) (2006) 5520–5529.
- [28] C. Delmas, M. Maccario, L. Croguennec, F. Le Cras, F. Weill, *Nature Mater.* 7 (8) (2008) 665–671.
- [29] C. Ramana, A. Mauger, F. Gendron, C. Julien, K. Zaghbi, J. Power Sources 187 (2) (2009) 555–564.
- [30] T. Zhang, M. Kamlah, *Contin. Mech. Thermodyn.* (2018) 1–20.
- [31] J.W. Cahn, J.E. Hilliard, *J. Chem. Phys.* 28 (2) (1958) 258–267.
- [32] G.K. Singh, G. Ceder, M.Z. Bazant, *Electrochim. Acta* 53 (26) (2008) 7599–7613.
- [33] D.A. Cogswell, M.Z. Bazant, *Nano Lett.* 13 (7) (2013) 3036–3041.
- [34] C.V. Di Leo, E. Rejovitzky, L. Anand, *J. Mech. Phys. Solids* 70 (2014) 1–29.
- [35] M.J. Welland, D. Karpeyev, D.T. O'Connor, O. Heinonen, *ACS Nano* 9 (10) (2015) 9757–9771.
- [36] G.F. Castelli, W. Dörfler, *PAMM* 21 (1) (2021) e202100169.
- [37] G.F. Castelli, L. von Kolzenberg, B. Horstmann, A. Latz, W. Dörfler, *Energy Technol.* 9 (6) (2021) 2000835.
- [38] T. Zhang, M. Kamlah, *J. Electrochem. Soc.* 165 (10) (2018) A1997–A2007.
- [39] T. Zhang, M. Kamlah, *Electrochim. Acta* 298 (2019) 31–42.
- [40] T. Zhang, M. Kamlah, *J. Electrochem. Soc.* 167 (2) (2020) 020508.
- [41] T. Zhang, M. Kamlah, *J. Power Sources* 483 (2021) 229187.
- [42] M. Huttin, M. Kamlah, *Appl. Phys. Lett.* 101 (13) (2012) 133902.
- [43] B. Han, A. Van der Ven, D. Morgan, G. Ceder, *Electrochim. Acta* 49 (26) (2004) 4691–4699.
- [44] P. Hohenberg, W. Kohn, *Phys. Rev.* 136 (3B) (1964) B864.
- [45] W. Kohn, L.J. Sham, *Phys. Rev.* 140 (4A) (1965) A1133.
- [46] P.E. Blöchl, *Phys. Rev. B* 50 (24) (1994) 17953.
- [47] G. Kresse, J. Hafner, *Phys. Rev. B* 47 (1) (1993) 558.
- [48] G. Kresse, J. Furthmüller, *Phys. Rev. B* 54 (16) (1996) 11169.
- [49] G. Kresse, D. Joubert, *Phys. Rev. B* 59 (3) (1999) 1758.
- [50] J.P. Perdew, K. Burke, M. Ernzerhof, *Phys. Rev. Lett.* 77 (18) (1996) 3865.
- [51] L. Wang, T. Maxisch, G. Ceder, *Phys. Rev. B* 73 (19) (2006) 195107.
- [52] G. Rousse, J. Rodriguez-Carvajal, S. Patoux, C. Masquelier, *Chem. Mater.* 15 (21) (2003) 4082–4090.
- [53] N.G. Hörmann, A. Groß, *Phys. Rev. Mater.* 3 (5) (2019) 055401.
- [54] N. Nadkarni, T. Zhou, D. Fraggadakis, T. Gao, M.Z. Bazant, *Adv. Funct. Mater.* (2019) 1902821.
- [55] O. Redlich, A. Kister, *Ind Eng Chem* 24 (1948) 345–352.
- [56] M.E. Gurtin, *Physica D* 92 (3–4) (1996) 178–192.
- [57] R. Malik, D. Burch, M. Bazant, G. Ceder, *Nano Lett.* 10 (10) (2010) 4123–4127.
- [58] R. Amin, P. Balaya, J. Maier, *Electrochem. Solid-State Lett.* 10 (1) (2006) A13.
- [59] L. Hong, L. Li, Y.-K. Chen-Wiegart, J. Wang, K. Xiang, L. Gan, W. Li, F. Meng, F. Wang, J. Wang, et al., *Nature Commun.* 8 (1) (2017) 1–13.
- [60] P. Bai, D.A. Cogswell, M.Z. Bazant, *Nano Lett.* 11 (11) (2011) 4890–4896.
- [61] M. Mykhaylov, M. Ganser, M. Klinsmann, F. Hildebrand, I. Guz, R. McMeeking, *J. Mech. Phys. Solids* 123 (2019) 207–221.
- [62] M. Ganser, F.E. Hildebrand, M. Klinsmann, M. Hanauer, M. Kamlah, R.M. McMeeking, *J. Electrochem. Soc.* 166 (4) (2019) H167.
- [63] H. Euchner, A. Groß, *Phys. Rev. Mater.* 6 (4) (2022) 040302.
- [64] Y. Zhu, Y. Xu, Y. Liu, C. Luo, C. Wang, *Nanoscale* 5 (2) (2013) 780–787.
- [65] N. Meethong, H.-Y. Huang, S.A. Speakman, W.C. Carter, Y.-M. Chiang, *Adv. Funct. Mater.* 17 (7) (2007) 1115–1123.
- [66] D. Gaston, C. Newman, G. Hansen, D. Lebrun-Grandie, *Nucl. Eng. Des.* 239 (10) (2009) 1768–1778.
- [67] J. Gaubicher, F. Boucher, P. Moreau, M. Cuisinier, P. Soudan, E. Elkaïm, D. Guyomard, *Electrochem. Commun.* 38 (2014) 104–106.